INTERNATIONAL JOURNAL FOR NUMERICAL METHODS IN FLUIDS
Int. J. Numer. Meth. Fluids **29**: 657–684 (1999)

THREE-DIMENSIONAL FINITE ELEMENT ANALYSIS OF TRANSIENT FLUID FLOW WITH FREE-SURFACE USING MARKER SURFACE METHOD AND ADAPTIVE GRID REFINEMENT

J.H. JEONG AND D.Y. YANG*

Department of Mechanical Engineering, Korea Advanced Institute of Science and Technology,
Taejon, Republic of Korea

SUMMARY

For three-dimensional finite element analysis of transient fluid flow with free-surface, a new marker surface method is proposed, in which the fluid flow is represented by the marker surface composed of marker elements instead of marker particles used in the marker particle method. This also involves an adaptive grid that is created under a new criterion of element categorization of filling states and the locations in the total region at each time step. The marker surface is used in order to represent the free-surface accurately, as well as to decrease the memory and computation time, and to effectively display the predicted three-dimensional free-surface. By using the adaptive grid in which the elements, finer than those in internal and external regions, are distributed in the surface region through refinement and coarsening procedures, the analysis of three-dimensional transient fluid flow with free-surface is achieved more efficiently. Through three-dimensional analysis of two kinds of problems using several grids, the efficiency of the proposed marker surface method and the adaptive grid are verified. Copyright © 1999 John Wiley & Sons, Ltd.

KEY WORDS: free surface; transient viscous incompressible fluid; finite element method; marker particle method; marker surface method; adaptive grid

1. INTRODUCTION

In order to accomplish the numerical analysis of fluid flow with free-surface, three approaches, namely the Lagrangian [1,2], the arbitrary Lagrangian–Eulerian (ALE) [3,4], and the Eulerian [5–10] methods have been developed successfully over the years. Among them, the Eulerian method has been widely used for analysis of general and complex problems since the remeshing procedure for a distorted mesh is not required. In this method, the Eulerian formulation and a fixed grid system are used, in which treatment of non-linear terms of the governing equation is necessary.

In the Eulerian method, the marker particle method and volume of fluid (VOF) method by Hirt *et al.* [8] are widely used to represent the fluid flow with free-surface. Typical examples of the marker particle method include the marker and cell (MAC) method by Harlow and Welch

---

* Correspondence to: Department of Mechanical Engineering, Korea Advanced Institute of Science and Technology, ME3214, 373-1, Kusong-dong, Yusong-gu, Taejon, 305-701, Republic of Korea. Tel.: + 82 42 8693214; fax: + 82 42 8693210; e-mail: dyyang@hanbit.kaist.ac.kr

CCC 0271–2091/99/060657–28$17.50

Received August 1997
Revised March 1998

[5] and the simplified marker and cell (SMAC) method [6], a revision of the MAC method. In the marker particle method, the phenomenon of fluid flow is represented by marker particles, and all elements of the total domain can be sorted into fluid elements that possess marker particles, and empty elements that do not. The fluid and empty regions of the total region are composed of the fluid and empty elements respectively. The marker particle has no mass and moves according to the velocity field. The velocity of the marker particle is obtained by interpolation of the nodal velocities of the element including the marker particle. The position of the free-surface and the flow phenomenon in the fluid region are represented by the distribution of marker particles. As merits of this method, the definition of the fluid region and free-surface are very simple and a visual display of the internal fluid flow is possible. However, the required memory and computational time may increase considerably for complex analysis, the definition of the free-surface is unclear, and the visual display of the free-surface is difficult in three-dimensional fluid flow problems. Numerical studies have been carried out to solve such problems. In order to reduce the required memory and computation time for two- and three-dimensional problems, Hwang and Stoehr [11] proposed the marker reduction technique, where the total number of marker particles can be decreased through deletion of marker particles in the internal fluid region, and Chen *et al.* [12] presented the surface marker (SM) method for two-dimensional problems in which a single string of marker particles along the

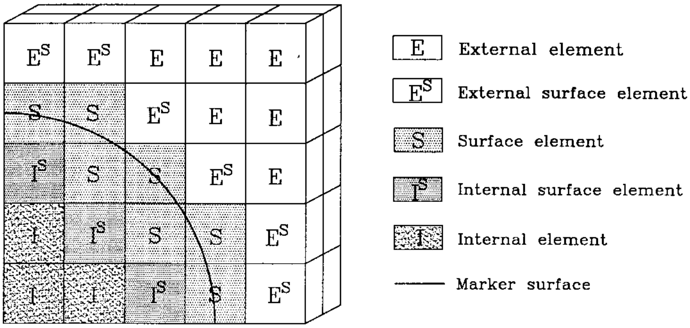

(a)

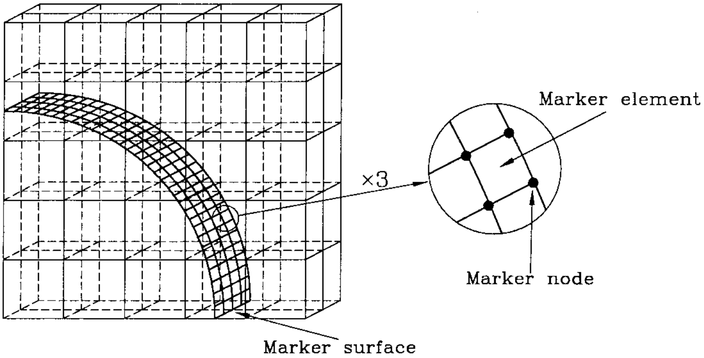

(b)

Figure 1. Element categorization of filling states and the locations in the total region (a) and schematic diagram of marker surface (b).

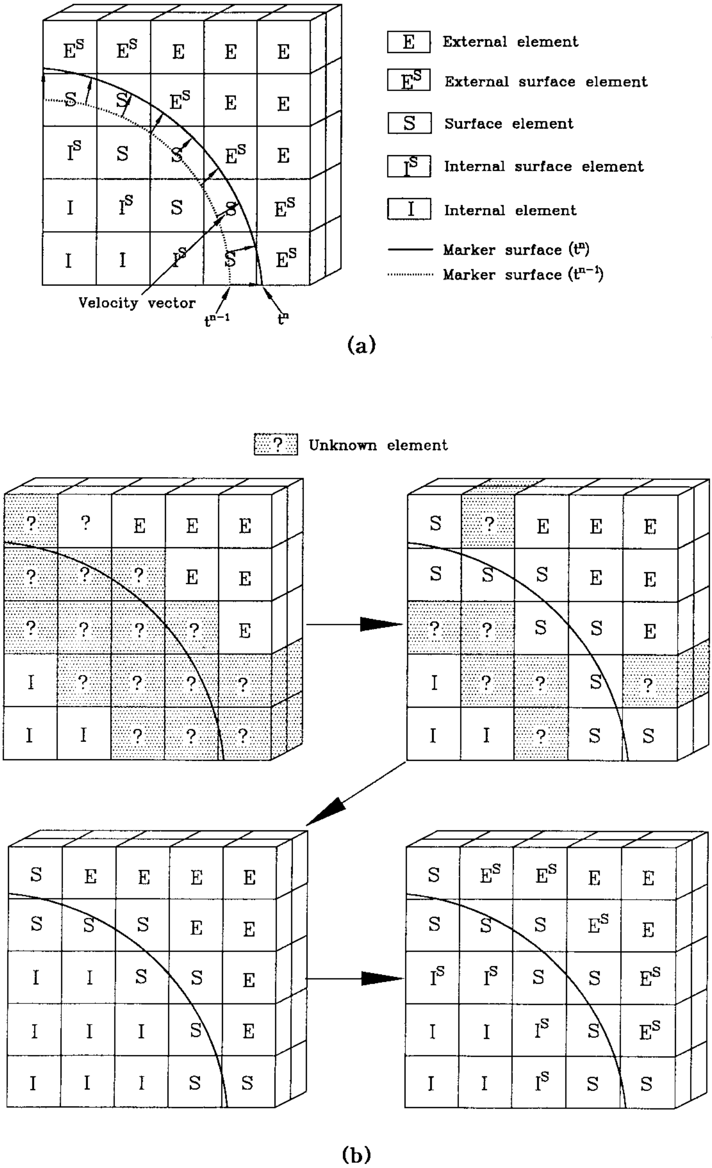

Figure 2. Categorization procedure for the fixed grid.

free-surface is used. In order to represent the two-dimensional free-surface more accurately, Wang and Stuhmiller [13] used linear surface segments to connect the marker particles in the modified partial cell method. In order to achieve an effective display of three-dimensional free-surface, Nichols and Hirt [14] used a display method where the surface configurations can be plotted by computing the elevation of the surface at each vertical grid line and a hidden-line perspective view. The aforementioned works provided effective numerical analysis of fluid flow with free-surface. However, the proposed methods have not been applied to three-dimensional finite element analysis with irregular grids.

Generally, the adaptive grid [15,16], created with an error indicator, has been applied to several fields of fluid flow analysis by using the finite element method, and its efficiency has been proven. Recently, Jeong and Yang [17] used the adaptive grid for the two-dimensional analysis of fluid flow with free-surface using the VOF method. However, the adaptive grid has not been used for three-dimensional analysis using the marker particle method. In the previous work using the marker particle method, the initial grid could not be adaptively altered during the analysis. Thus, the quality of the initial grid was critical, and in order to improve the accuracy of numerical results, the required computation time and memory size had to be increased by geometric progression, since the total number of elements of the grid for finite element method (FEM) analysis was increased.

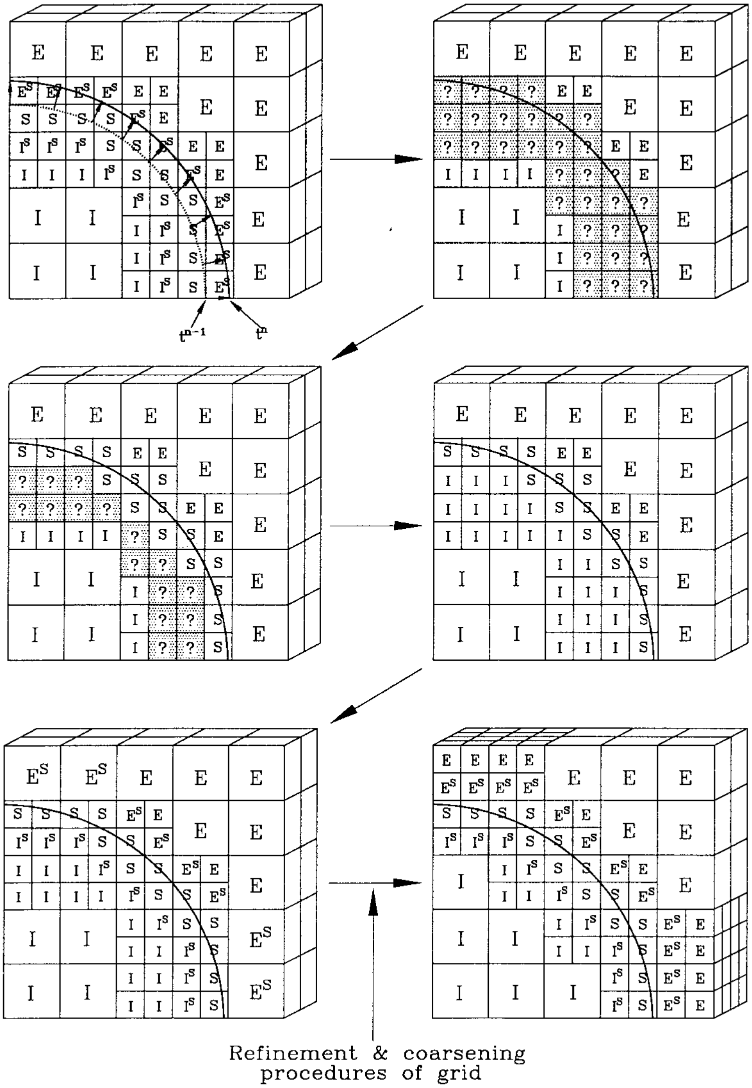

Figure 3. Categorization procedure for the adaptive grid.

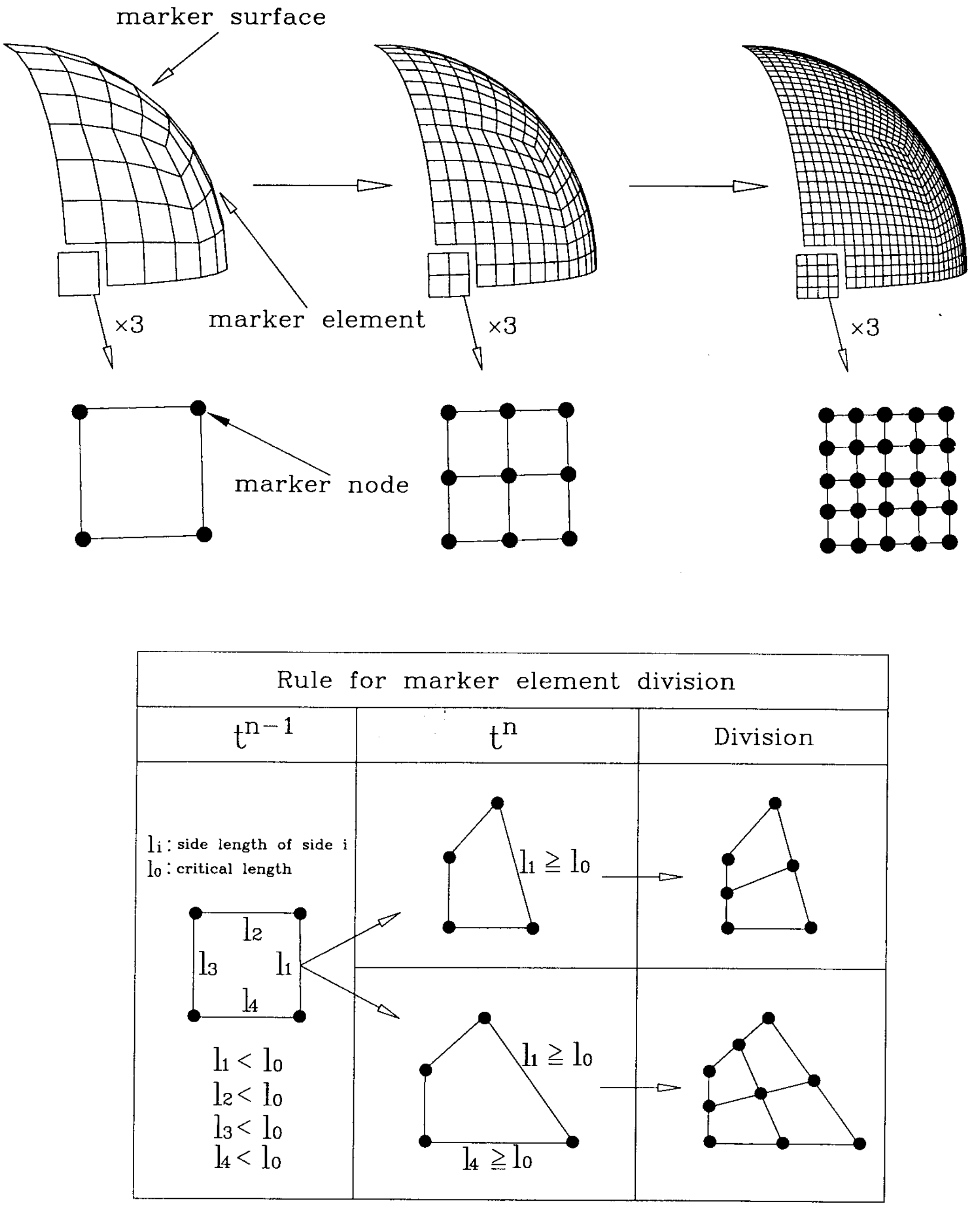

Figure 4. Marker surface refinement procedure.

In this study to carry out a finite element analysis of three-dimensional fluid flow with free-surface more effectively, a marker surface method, in which the fluid flow is represented by a marker surface composed of the marker elements instead of marker particles, is proposed incorporating an adaptive grid that is created under a new criterion of element categorization of filling states and the locations in the total domain at each time step. The marker surface method was developed to predict the free-surface more accurately, to decrease the memory and computation time, and to display the predicted free-surface in a three-dimensional co-ordinate system. In addition, an adaptive grid incorporated into the marker surface method is created at each time step through grid refinement and coarsening procedures, as opposed to having a fixed grid as in the marker particle method. In the adaptive grid, the elements finer than those of the internal and external regions are distributed over the surface region. The adaptive grid is applied to generate a flow field that better resembles the shape of the predicted free-surface at each time step, and to advance the predicted free-surface more precisely. Here, the flow field means the grid generated from the adaptive grid to obtain the velocity field by a FEM analysis. The Navier–Stokes and continuity equations form the governing equations, the penalty and predictor–corrector methods are used for the FEM formulation, and the grid of the total domain is composed of hexahedron elements. By using the marker surface method and adaptive grid refinement, the three-dimensional radial flow with a point source and the collapse of a dam were analyzed and compared with the known theoretical solutions and the experimental results. In order to verify the efficiency of this method, numerical analyses were also carried out for several cases using different grids.

2. GOVERNING EQUATIONS

For the three-dimensional analysis of the transient incompressible viscous flow with free-surface, the continuity equation and the Navier–Stokes equation are used as governing equations in the rectangular Cartesian co-ordinate system.

Continuity equation:

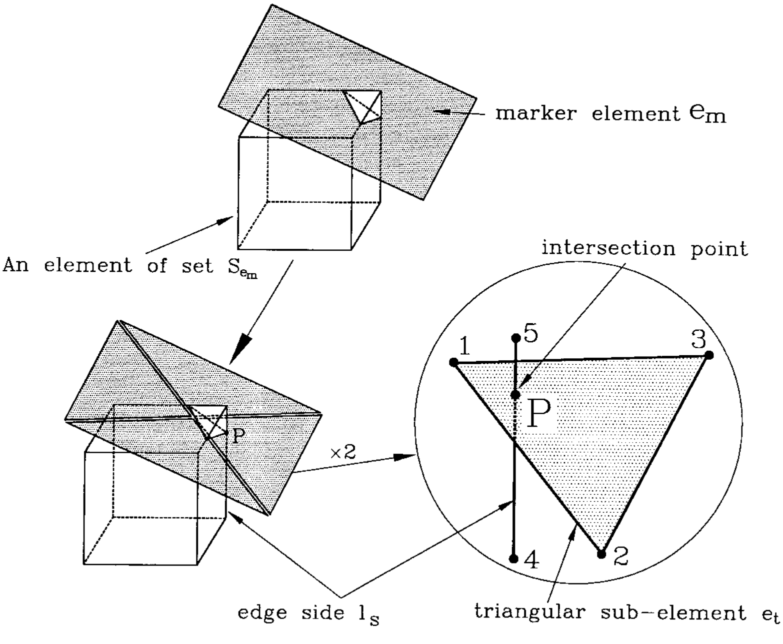

Figure 5. Sequence of intersection check.

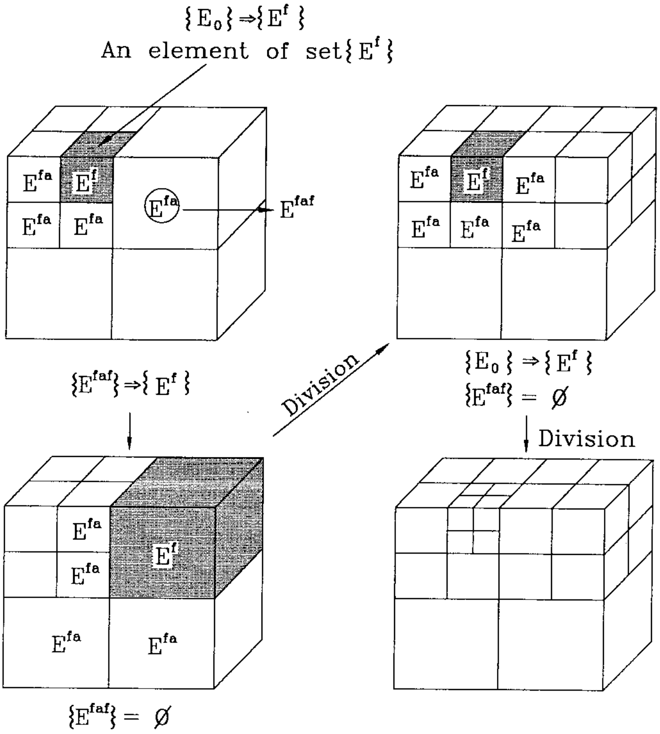

Figure 6. Sequence of divisions for refinement.

$$\frac{\partial u_i}{\partial x_i} = 0 \quad \text{in} \quad \Omega. \tag{1}$$

Navier–Stokes equation:

$$\rho \frac{\partial u_i}{\partial t} + \rho u_j \frac{\partial u_i}{\partial x_j} = \frac{\partial}{\partial x_j} \boldsymbol{\sigma}_{ji}(u) + \rho f_i \quad \text{in} \quad \Omega, \tag{2}$$

where

$$\boldsymbol{\sigma}_{ij} = -p\delta_{ij} + 2\mu \boldsymbol{d}_{ij}, \qquad \boldsymbol{d}_{ij} = \frac{1}{2}\left(\frac{\partial u_i}{\partial x_j} + \frac{\partial u_j}{\partial x_i}\right).$$

In the above equations, $i = 1, 2, 3$, $j = 1, 2, 3$ and t, u_i, p, ρ, μ and f_i are the time, velocity component in the x_i-direction, pressure, density, dynamic viscosity and body force respectively, and $\boldsymbol{\sigma}_{ij}$ and $\boldsymbol{d}_{ij}$ denote the stress and the strain tensors respectively.

On the free-surface $\partial\Omega_{\mathrm{s}}$, the surface tension, the viscous stress and the outside gas pressure are assumed to be zero, the free-slip condition is applied to the wall boundary $\partial\Omega_{\mathrm{wall}}$ and the essential boundary condition is imposed on the inflow boundary $\partial\Omega_{\mathrm{inflow}}$ as follows:

$$\text{On } \partial\Omega_{\mathrm{s}}, \quad \sigma_{\mathrm{n}} = -p + 2\mu_{\mathrm{air}} \frac{\partial u_{\mathrm{n}}}{\partial x_{\mathrm{n}}} = 0, \qquad \tau = \mu_{\mathrm{air}}\left(\frac{\partial u_{\mathrm{n}}}{\partial x_{\mathrm{t}}} + \frac{\partial u_{\mathrm{t}}}{\partial x_{\mathrm{n}}}\right) = 0,$$

$$\text{On } \partial\Omega_{\mathrm{wall}}, \quad u_{\mathrm{nw}} = 0,$$

$$\text{On } \partial\Omega_{\mathrm{inflow}}, \quad u_i = \overline{u_i},$$

where σ_n, τ, μ_{air}, subscripts n and t denote the normal stress, shear stress, dynamic viscosity of air, and the normal and tangential directions of the free-surface; u_{n_w} is the normal velocity component at the wall boundary, and $\bar{u}_i$ is the velocity component given at the inflow boundary.

3. FINITE ELEMENT FORMULATION

By using the penalty-function formulation and the Galerkin formulation [18,19], the Navier–Stokes equation and the continuity equation are discretized. In the penalty-function formulation of the incompressibility constraint, the continuity equation (1) is replaced by

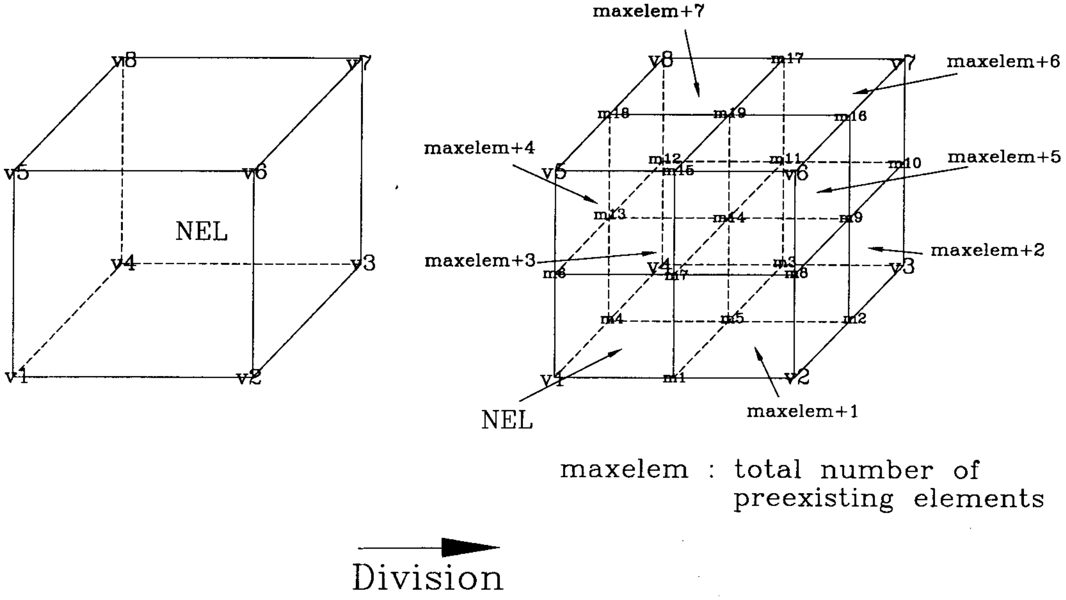

element number	connectivity
nel	[v1, m1, m5, m4, m6, m7, m14, m13]
maxelem+1	[m1, v2, m2, m5, m7, m8, m9, m14]
maxelem+2	[m5, m2, v3, m3, m7, m8, m9, m14]
maxelem+3	[m4, m5, m3, v4, m13, m14, m11, m12]
maxelem+4	[m6, m7, m14, m13, v5, m15, m19, m18]
maxelem+5	[m7, m8, m9, m14, m15, v6, m16, m19]
maxelem+6	[m14, m9, m10, m11, m19, m16, v7, m17]
maxelem+7	[m13, m14, m11, m12, m18, m19, m17, v8]

Figure 7. Division procedure of an element.

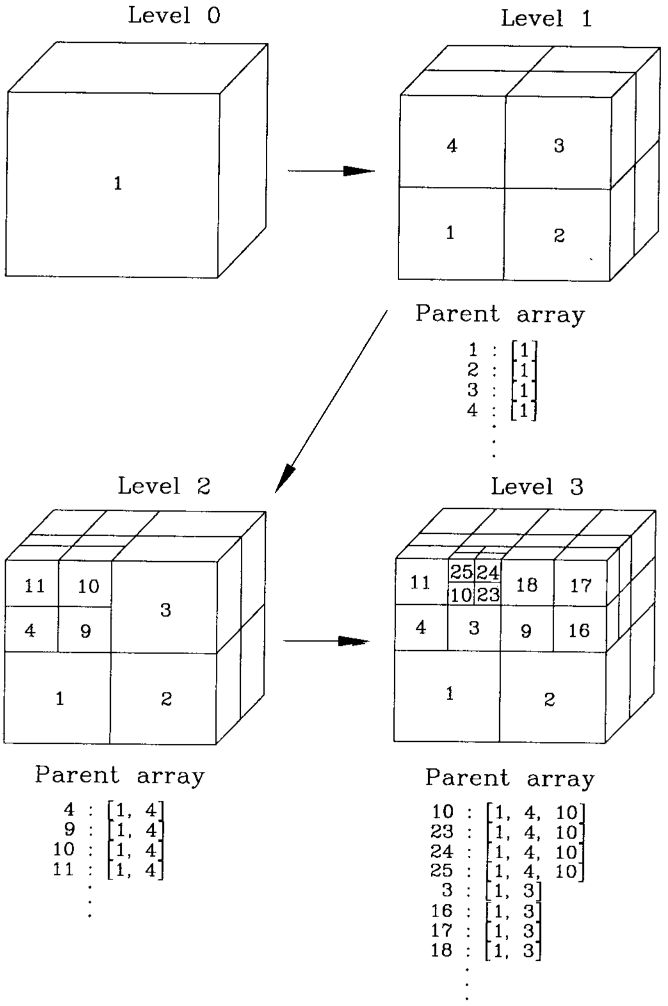

Figure 8. Generation of parent array.

$$\frac{\partial u_i}{\partial x_i} + \frac{p}{\lambda} = 0. \tag{4}$$

From Equation (4), the constitutive equation is replaced by

$$\boldsymbol{\sigma}_{ij} = \lambda d_{kk}\delta_{ij} + 2\mu \boldsymbol{d}_{ij} \tag{5}$$

where λ is the penalty constant to be positive and sufficiently large.

In the Galerkin formulation of Equations (2) and (5), the weak form is obtained as follows:

$$\int_\Omega (\rho \dot{u}_i \bar{u}_i + \rho u_j u_{i,j} \bar{u}_i + \lambda u_{j,j} \bar{u}_{i,i} + 2\mu u_{i,j} \bar{u}_{i,j})\, \mathrm{d}\Omega = \int_\Omega \rho f_i \bar{u}_i \, \mathrm{d}\Omega. \tag{6}$$

Here, the term with λ is integrated by using a reduced integration technique. Then, the weak form is discretized and the finite element equation becomes

$$M_{i_\alpha j_\beta} \dot{U}_{j_\beta} + C_{i_\alpha j_\beta} U_{j_\beta} + N(u_i)_{i_\alpha} = F_{i_\alpha}, \tag{7}$$

where,

$$M_{i_\alpha j_\beta} = \int \rho N_\alpha N_\beta \delta_{ij} \, d\Omega,$$

$$C_{i_\alpha j_\beta} = \int \{\lambda N_{\alpha,i} N_{\beta,j} + \mu N_{\alpha,j} N_{\beta,i} + \mu \delta_{ij} N_{\alpha,k} N_{\beta,k}\} \, d\Omega,$$

$$N(u_i)_{i_\alpha} = \int \rho \delta_{ij} N_\alpha u_k u_{i,k} \, d\Omega,$$

$$F_{i_\alpha} = \int N_\alpha f_i \, d\Omega,$$

$U_{k\gamma}$: nodal value of u_k, $\alpha = 1, 2, \ldots, 8$; $\beta = 1, 2, \ldots, 8$.

Equation (7) is solved by using the predictor–corrector method [17,18] as a time stepping algorithm.

4. COMPUTATIONAL PROCEDURE

Whereas the marker particles are distributed over the three-dimensional fluid region in the marker particle method, only the marker surface representing the predicted free-surface is directly used in the proposed method, such that the required computation time and memory size are considerably decreased. The marker surface can be further used for the refinement

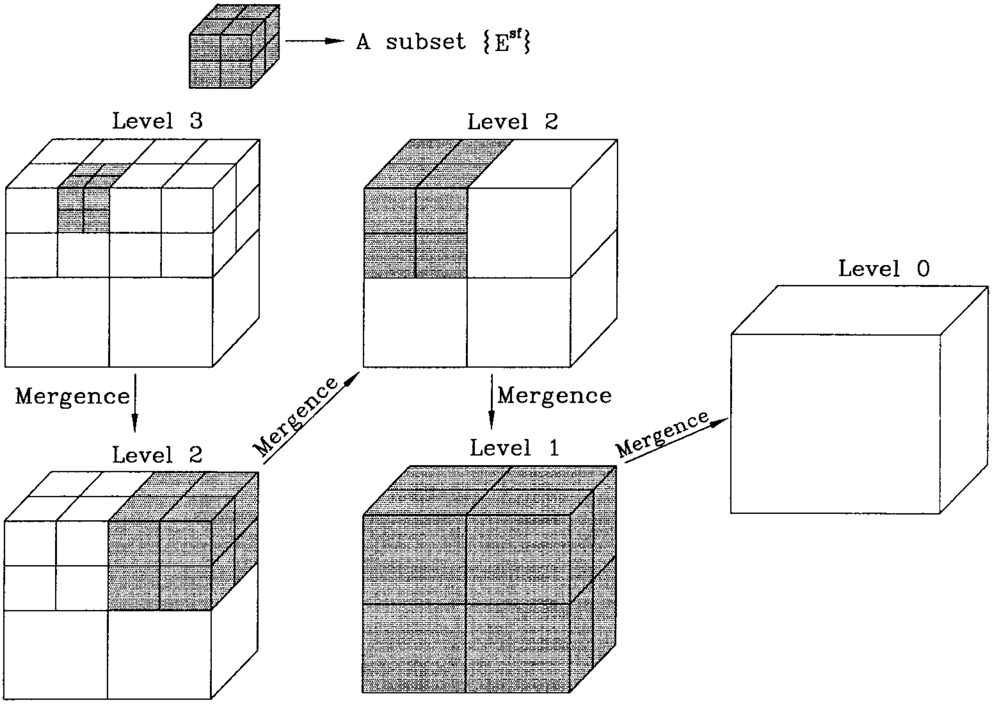

Figure 9. Sequence of mergences for coarsening.

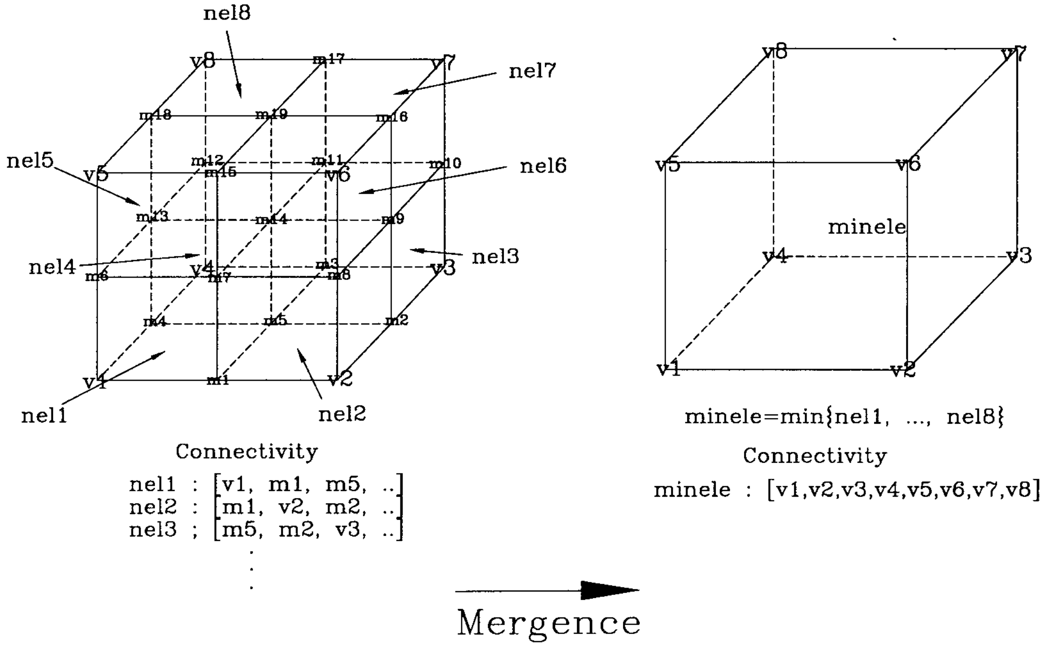

Figure 10. Mergence procedure of eight subelements.

procedure and hidden-line treatment. When an expansion flow occurs locally or globally, some marker elements can be coarse. In this case, in order to maintain the accuracy of the predicted free-surface at each time step, each of the coarse marker elements should be divided into two or four subelements by the marker surface refinement procedure. It is also possible to display the predicted free-surface by the hidden-line removal treatment in a three-dimensional co-ordinate system. In the preprocessing stage for numerical analysis, the initial grid and marker surface are generated, and values for the surface refinement level, material properties,

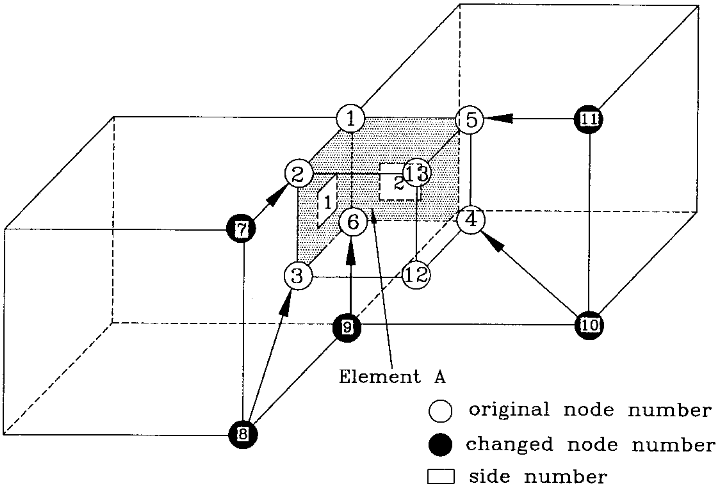

Figure 11. Configurations of disconnected sides and nodes.

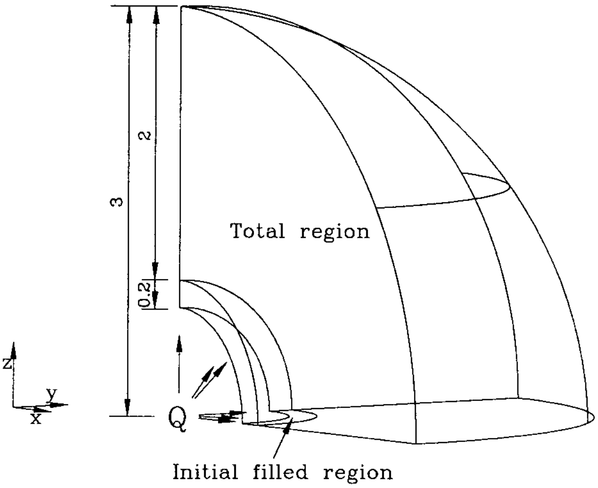

Figure 12. Schematic diagram of total and initial filled regions, and inflow boundary condition.

boundary conditions, and initial element types are specified. Then, the time step is increased, and by the grid refinement and coarsening procedures, the adaptive grid is generated, which leads to the creation of the grid of the flow field for a FEM analysis. Next, the velocity and pressure fields are obtained from the FEM analysis. Then, the marker surface is advanced according to the velocity field, and the marker elements are refined through the marker surface refinement procedure. This procedure is iterated until the current filling time reaches the total time. The procedure for creating the adaptive grid can be divided into two procedures, namely grid refinement and grid coarsening. The procedures for the marker surface method and generation of the adaptive grid are illustrated in detail in the following.

4.1. Procedure for marker surface method

Step I: The initial marker surface is generated as shown in Figure 1. The side length of the marker element should be short enough to represent the initial free-surface.

Step II: As shown in Figure 1(a), all initial elements are sorted into five types: the internal element, internal surface element, surface element, external surface element and external element, where the internal surface and external surface elements are adjacent to the surface elements. The inside regions of the internal elements and internal surface elements, the surface elements, and the external elements and external surface elements are respectively, filled with fluid, completely filled, partially filled, and empty. In addition, the internal and internal surface elements can contain any part or no part of the marker surface, the surface element must contain any part of the marker surface, and the external surface and external elements should contain no part of the marker surface. The grid of the flow field is composed of the internal element, internal surface element, and surface element. At the next time step, the marker surface is moved inside the surface region composed of the internal surface, surface and external surface elements, because the marker surface is prevented from moving too far from the current position. If the above condition is not satisfied in any part of the marker surface, then the value of the given time increment must be decreased.

Step III: As shown in Figure 2(a), the co-ordinates of marker nodes are updated as follows:

$$x_m^{n+1} = x_m^n + u_m^{n+1}\Delta t, \tag{8}$$

where x_m^{n+1} and x_m^n are the co-ordinates of marker node m at the time steps $n+1$ and n respectively, and u_m^{n+1} is the velocity of marker node m at the time step $n+1$. Here, the velocity u_m^{n+1} is obtained by interpolation of the nodal velocities of the element containing marker node m.

Step IV: The type of an element is changed according to the movement of the marker surface. First, as shown in Figure 2(b), the internal surface element, surface element and external surface element at time step $n-1$ are categorized into a newly defined set of unknown elements. Then, among the unknown elements, the elements that comprise any part of the marker surface at time step n become surface elements. The remaining unknown elements are categorized according to the state of their neighboring elements. If an unknown element is adjacent to an external one, then the unknown element is changed into an external element. Likewise, if an unknown element is adjacent to an internal element, it becomes an internal element. This procedure is repeated until no unknown element exists.

When no unknown element remains, the sets of internal surface and external surface elements are obtained by checking the categories of neighboring elements. If an internal element is adjacent to a surface element, then it is changed into an internal surface element, and if an external element is adjacent to a surface element, then it becomes an external surface element. An internal element contains mainly no part of the marker surface. The internal element may however, contain any part of the marker surface, when the flection of the marker surface is serious or a folding phenomenon occurs. This procedure can be also achieved for the adaptive grid as shown in Figure 3.

Step V: Due to movement of the marker surface, the shape and size of marker elements are changed and some marker elements may become coarse. In this case, the procedure of the marker surface refinement is carried out. The refinement procedure is determined by the side length of the marker element. If the side length is longer than the given critical length, the marker element is divided into two or four subelements. As shown in Figure 4, if the length of sides 1 or 3 is longer than the given critical length, and the lengths of sides 2 and 4 are shorter than the given critical length, then two new nodes at the middle of the sides 1 and 3 are generated, and the marker element is divided into two marker elements. In another case,

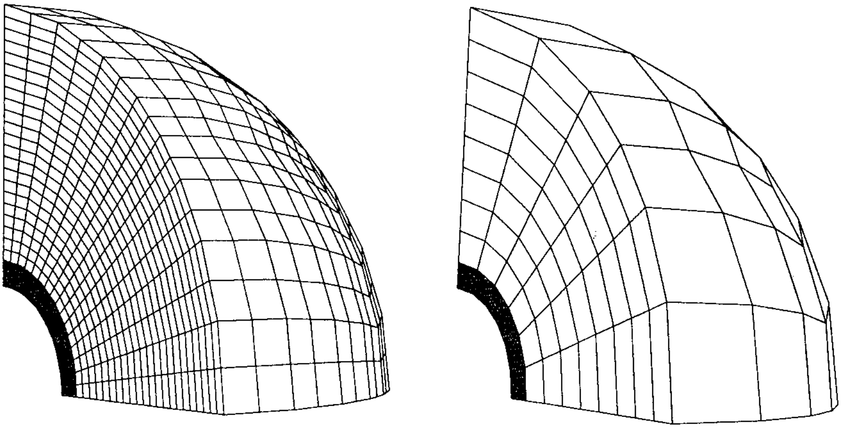
(a) (b)

Figure 13. Initial grids and filled regions in cases I (a) and II (b).

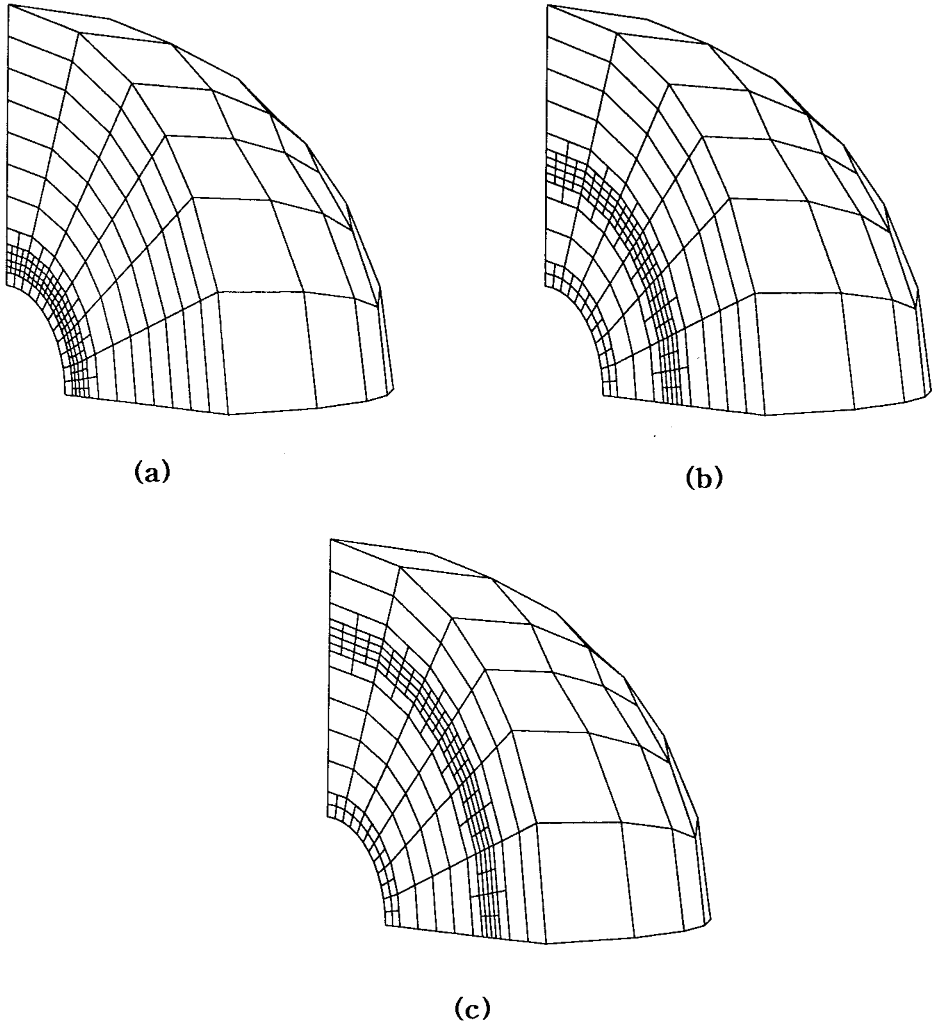

Figure 14. Adaptive grids at $t = 0$ (a), 1.5 (b) and 3.5 (c) obtained in case II.

if the lengths of sides 1 or 3 and sides 2 or 4 are longer than the critical length, then new nodes are generated at the middle of all four sides and at the center of the marker element to divide the marker element into four marker elements. In order to represent the free-surface accurately, the critical side length should be shorter than the minimum length of edge sides of elements of the total region grid. Nodal numbers are newly given or are determined to be equivalent to a pre-existing node by comparing its co-ordinates with others.

4.1.1. Check of intersection. In order to check whether an element is composed of any part of the marker surface, a procedure of checking the intersection between the marker surface and elements is required. This procedure is expressed as follows.

Step 1: A search is carried out to determine the elements containing one or several marker nodes and each marker node is stored with the data of the element number to which it belongs.

Step 2: As shown in Figure 5, for efficient searching, each marker element is divided into four triangular subelements, each of which forms a plane.

Step 3: In considering a marker element e_m, the set s_{e_m}, which includes the surrounding elements of e_m that contain no marker node, is determined. The elements of s_{e_m} can be obtained efficiently from the neighboring elements of the elements that contain the marker nodes of e_m. Each triangular subelement of the marker element and each edge side of elements belonging to s_{e_m} are checked to determine whether any intersection occurs. As shown in Figure 5, when a triangular subelement e_t and edge side l_s are considered, the plane equation of e_t is expressed as follows:

$$ax + by + cz + d = 0, \tag{9}$$

where a, b, c, and d are constants that are obtained as follows:

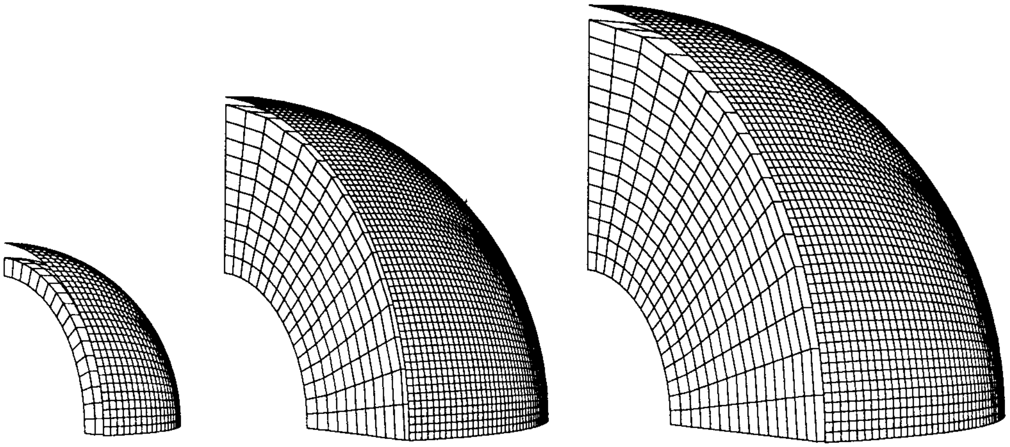

Case I

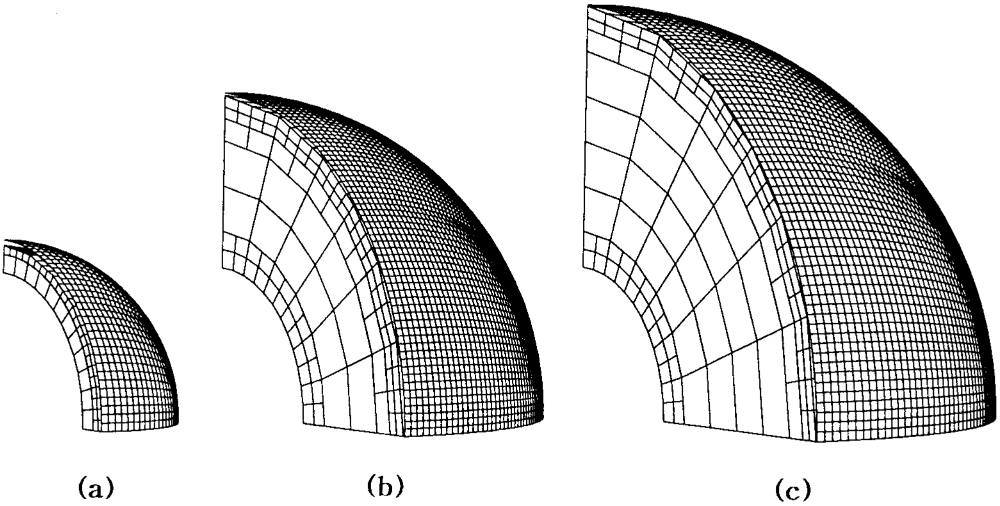

Case II

Figure 15. Predicted free-surfaces and element configurations at $t = 1.5$ (a), 2.5 (b) and 3.5 (c) s obtained in cases I and II.

Table I. Comparison of results obtained in all cases

	Fixed grid	Adaptive grid
Grid of flow field		
Average total number of elements	2158	1528
Average total number of nodes	2659	2272
Grid of total region		
Average total number of elements	4608	2466
Average total number of nodes	5425	3321
Relative length of edge side of element in front region		
γ-direction	1.5	1
θ-direction	1.5	1
ϕ-direction	1.5	1
Relative total time	1.1	1

$$a=1,\quad b=0,\quad c=0,\quad d=-x'_1 \quad \text{when } x'_1=x'_2=x'_3,$$

$$a=0,\quad b=1,\quad c=0,\quad d=-y'_1 \quad \text{when } y'_1=y'_2=y'_3,$$

$$a=0,\quad b=0,\quad c=1,\quad d=-z'_1 \quad \text{when } z'_1=z'_2=z'_3,$$

$$a=0,\quad b=1,\quad c=\frac{y'_2-y'_1}{z'_1-z'_2},\quad d=-(y'_1+cz'_1) \quad \text{when } D=0 \quad \text{and} \quad z'_1\neq z'_2,$$

$$a=0,\quad b=1,\quad c=\frac{y'_3-y'_2}{z'_2-z'_3},\quad d=-(y'_2+cz'_2) \quad \text{when } D=0 \quad \text{and} \quad z'_2\neq z'_3,$$

$$a=0,\quad b=1,\quad c=\frac{y'_1-y'_3}{z'_3-z'_1},\quad d=-(y'_3+cz'_3) \quad \text{when } D=0 \quad \text{and} \quad z'_3\neq z'_1,$$

$$a=1,\quad b=\frac{D_b}{D},\quad c=\frac{D_c}{D},\quad d=\frac{D_d}{D} \quad \text{in other cases;}$$

$$D=y'_1\begin{vmatrix} z'_2 & 1 \\ z'_3 & 1 \end{vmatrix} - z'_1\begin{vmatrix} y'_2 & 1 \\ y'_3 & 1 \end{vmatrix} + \begin{vmatrix} y'_2 & y'_2 \\ y'_3 & y'_3 \end{vmatrix},$$

$$D_b=\begin{vmatrix} -x'_1 & z'_1 & 1 \\ -x'_2 & z'_2 & 1 \\ -x'_3 & z'_3 & 1 \end{vmatrix},\qquad D_c=\begin{vmatrix} y'_1 & -x'_1 & 1 \\ y'_2 & -x'_2 & 1 \\ y'_3 & -x'_3 & 1 \end{vmatrix},\qquad D_d=\begin{vmatrix} y'_1 & z'_1 & -x'_1 \\ y'_2 & z'_2 & -x'_2 \\ y'_3 & z'_3 & -x'_3 \end{vmatrix}$$

where $x'_i=x_i-x_4$, $y'_i=y_i-y_4$ and $z'_i=z_i-z_4$, and x_i, y_i and z_i are the co-ordinates of point i. Then, the intersection point P of e_t and l_s is derived as follows:

$$x_p=-\frac{x'_5d}{ax'_5+by'_5+cz'_5},\quad y_p=-\frac{y'_5d}{ax'_5+by'_5+cz'_5},\quad z_p=-\frac{z'_5d}{ax'_5+by'_5+cz'_5}. \tag{10}$$

Finally, the following conditions must be satisfied in order for point P to be located on l_s and e_t.

$$|\vec{a}_{5p}| + |\vec{a}_{4p}| = |\vec{a}_{54}| \text{ on segment } l_s$$

$|\vec{a}_{1p} \times \vec{a}_{2p}| + |\vec{a}_{2p} \times \vec{a}_{3p}| + |\vec{a}_{3p} \times \vec{a}_{1p}| = |\vec{a}_{21} \times \vec{a}_{31}|$ on triangular element e_t, where $\vec{a}_{ij}$ is a vector represented by components $(x_i - x_j)$, $(y_i - y_j)$, $(z_i - z_j)$.

4.2. Grid refinement procedure for adaptive grid

The grid refinement procedure can be divided into two steps. The first step is the selection procedure, in which the set of elements to be divided is selected. The second step is the division procedure, in which the selected elements are divided. For the grid refinement procedure, the element numbers of neighboring elements and the refinement level of each element are stored. There are six face sides and 12 edge sides in a hexahedron element, and the maximum total number of neighboring elements for each element is 48. The refinement procedure is accomplished incrementally from the minimum level to the maximum level by the refinement loop. The selection and division procedures are explained in detail below.

4.2.1. Selection procedure for refinement. Step 1: By the refinement criterion, a set $\{E_0\}$ is obtained as shown in Figure 6. The set $\{E_0\}$ is the set of elements to be divided. The criterion for refinement is the element category. If the category of an element is internal surface, surface, or external surface element, and the refinement level of the element is equal to the current level of the refinement loop, then the element belongs to $\{E_0\}$. Then a set $\{E^f\}$ is initialized by $\{E_0\}$.

Step 2: The set $\{E^{faf}\}$ is obtained from the single level rule, which indicates that when an element A is considered, the absolute difference between the level of A and the level of each neighboring element must be zero or 1. When an element B belonging to $\{E^f\}$ is divided into eight subelements, and a neighboring element of B does not satisfy the single level rule, then the neighboring element belongs to $\{E^{faf}\}$. If $\{E^{faf}\}$ is not a null set then $\{E^f\}$ is replaced by $\{E^{faf}\}$, and this procedure is repeated until $\{E^{faf}\}$ becomes a null set. Then, the division procedure for $\{E^f\}$ can be carried out, and $\{E^f\}$ is initialized by $\{E_0\}$. This initialization process is repeated until the division procedure for $\{E_0\}$ is completely accomplished.

4.2.2. Division procedure. When the set $\{E^f\}$ is obtained by the selection procedure explained above, each element belonging to $\{E^f\}$ is divided into eight subelements. The division procedure is explained as follows.

Step 1: As shown in Figure 7, when an element NEL is divided, 19 new nodes, $m1 \ldots m19$, are generated at the middle of the edge and face sides and at the center of the element.

Step 2: The co-ordinates of the newly generated 19 nodes are checked with existing nodes. If the node is coincident, the nodal number of the pre-existing node is given, otherwise a new nodal number is given.

Step 3: The connectivities of the eight subelements are created as shown in Figure 7, and the total number of elements is increased by 7 from the previous value.

Step 4: The data of the neighbor array and the constrained side array are updated. Here, the neighbor array is the array that stores the element numbers of neighboring elements for each element, and the constrained side array is the array that stores the number of the sides with disconnected nodes.

Step 5: The numerical data for the eight subelements and new nodes are calculated. The nodal velocity and pressure are determined by interpolation of the nodal values of the parent element. The refinement level of each subelement is given by that of the parent element plus one. The boundary condition is also updated. In particular, the element number of the parent element is stored in the parent array for the coarsening procedure, as shown in Figure 8.

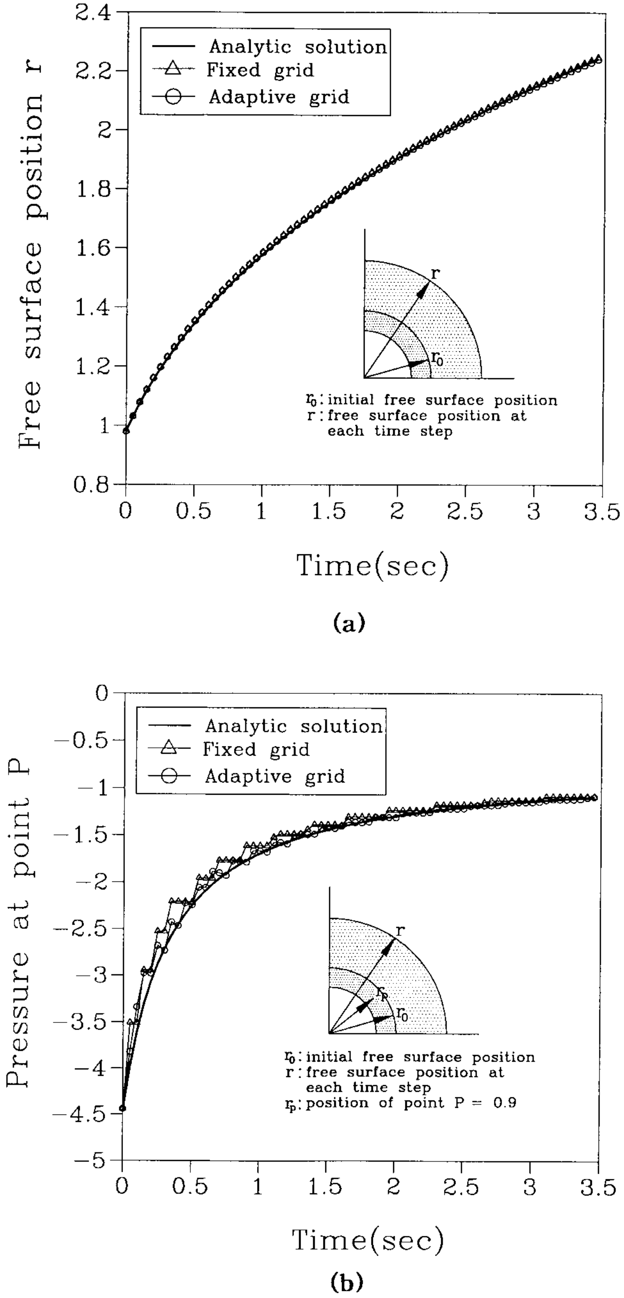

Figure 16. Positions of predicted free-surfaces (a) and pressures (b) vs. time compared with theoretical solutions in both cases.

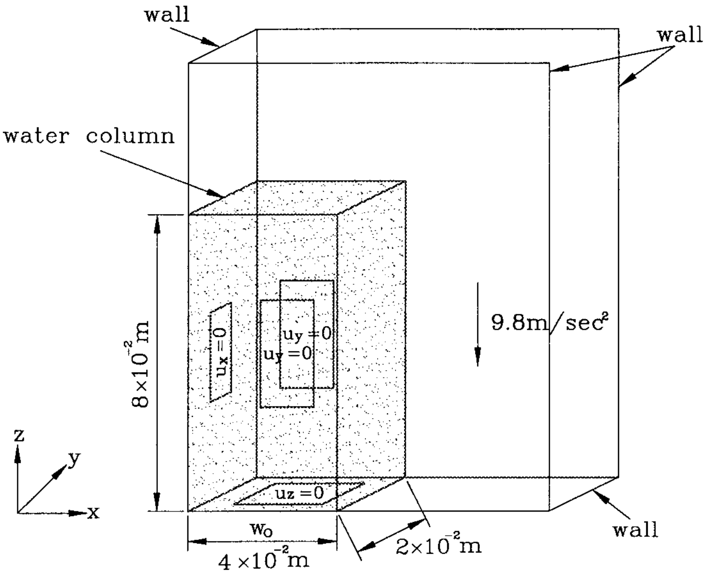

Figure 17. Schematic diagram of initial water column.

4.3. *Grid coarsening procedure for adaptive grid*

Similar to the grid refinement procedure, the coarsening procedure is composed of two steps. The first step is the selection procedure to obtain the whole set of subsets to be merged, and the second step is the mergence procedure that merges the eight subelements into an element. The coarsening procedure is accomplished incrementally from the maximum level to the minimum level. The selection for coarsening and mergence procedures are explained below.

4.3.1. Selection procedure for coarsening. Step 1: As shown in Figure 9, the set $\{\{E^{sf}\}\}$ of the subsets $\{E^{sf}\}$s, is obtained by a coarsening criterion. A subset $\{E^{sf}\}$ includes the eight elements that are to be merged into an element. The coarsening criterion is the element category as was the case for grid refinement. If an element, whose refinement level equals the current level of the coarsening loop, is an internal or external element, then it belongs to the temporary set $\{E^{\mathrm{temp}}\}$, which is used for the next sorting procedure. Then, the elements belonging to $\{E^{\mathrm{temp}}\}$ are sorted into subsets, $\{E^{\mathrm{t}sf}\}$, with each subset being composed of elements divided from a parent element. The maximum total number of the elements belonging to each $\{E^{\mathrm{t}sf}\}$ is 8.

Step 2: If the total number of elements belonging to a $\{E^{\mathrm{t}sf}\}$ is 8 and an element merged from eight elements belonging to $\{E^{sf}\}$ satisfies the single level rule, then the subset $\{E^{\mathrm{t}sf}\}$ becomes the subset $\{E^{sf}\}$.

4.3.2. Mergence procedure. When the set $\{\{E^{sf}\}\}$ is obtained by the selection procedure explained above, the eight elements belonging to each $\{E^{sf}\}$ are merged into an element. The mergence procedure is explained as follows:

Step 1: As shown in Figure 10, the vertex nodes of a newly merged element are obtained from the nodes belonging to the eight elements. The nodes, other than the vertex nodes, are eliminated or left in place by checking whether neighboring elements include them.

Step 2: The minimum value of element numbers of the eight elements is assigned to that of the newly merged element. Its connectivity is created as shown in Figure 10. The connectivities and element numbers of the eight subelements and the useless nodal numbers are eliminated from each array. The total number of elements decreases by 7 from the previous value.

Step 3: The data of the neighbor array, constrained side array and parent array are updated.

Step 4: The numerical data for the newly merged element are calculated. The refinement level of the newly merged element is assigned the refinement level value of the subelement minus one. The boundary condition is updated.

4.3.3. Treatment for disconnected nodes. The grid of the flow field generated from an adaptive grid may include disconnected nodes. In considering element A, as shown in Figure 11, the following constraint equation is used to treat the disconnected edge midnodes, 2, 5 and 6, and face midnodes, 3 and 4.

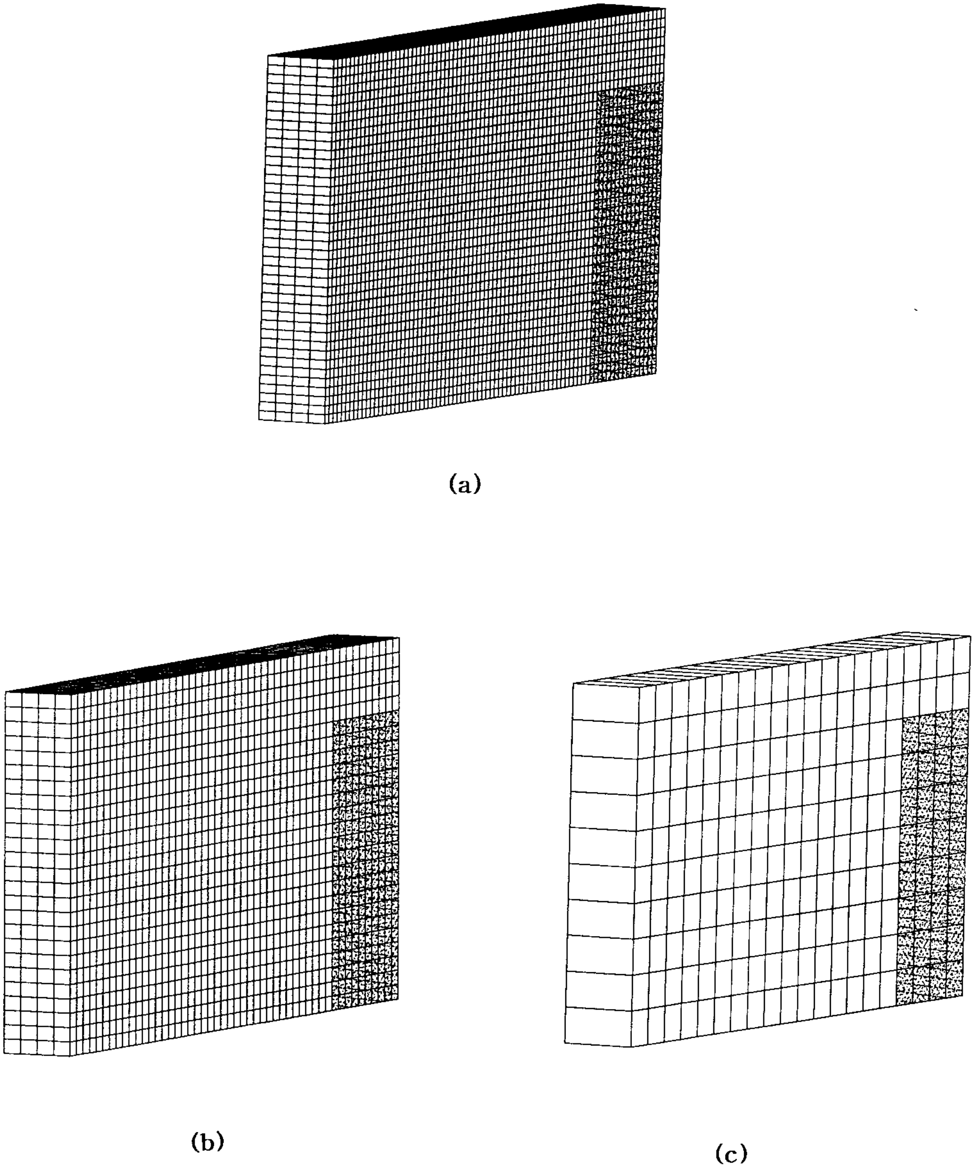
(a)

(b)

(c)

Figure 18. Initial grids and initial filled regions in cases I (a), II (b) and III (c).

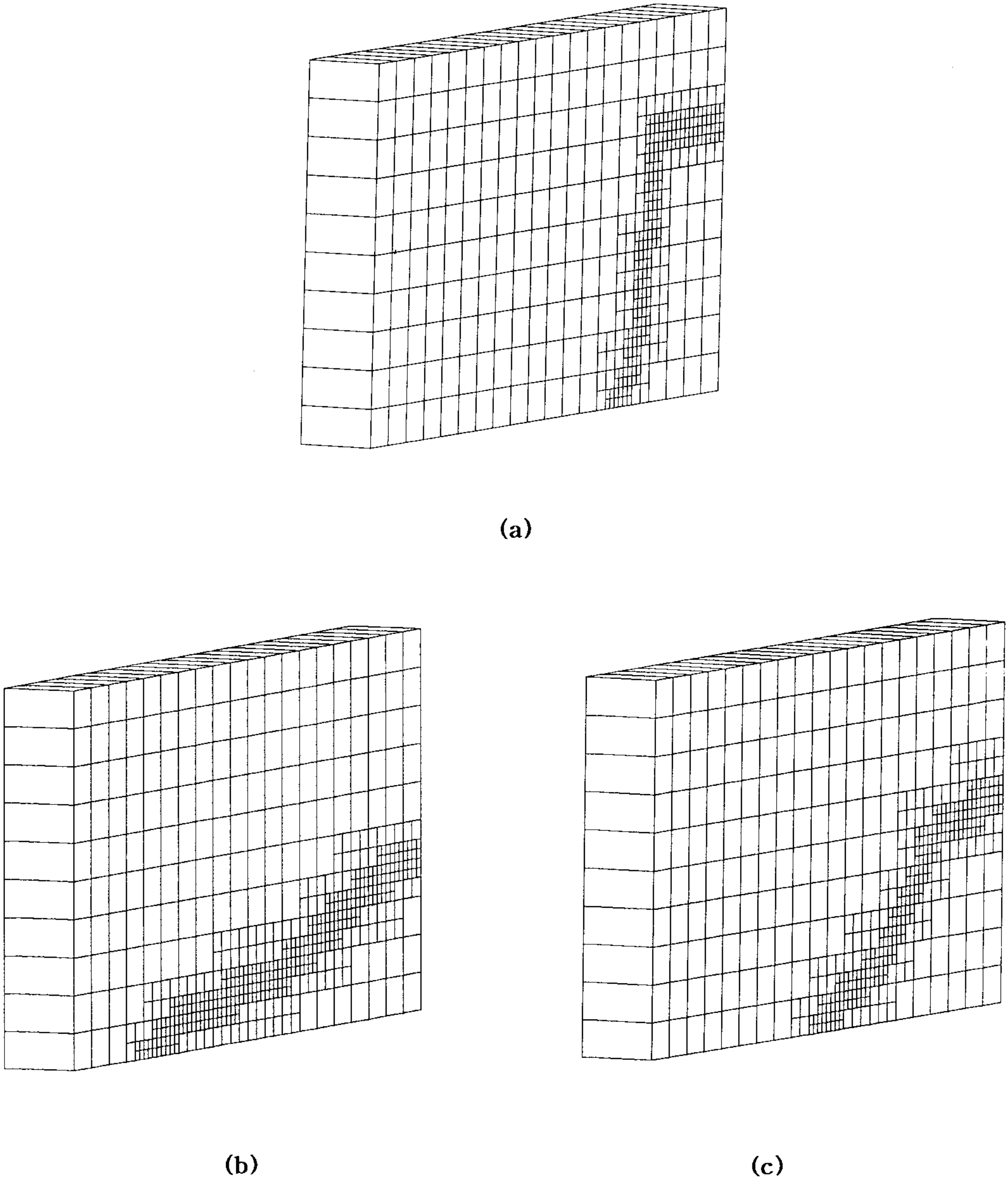
(a)

(b)

(c)

Figure 19. Adaptive grids at $T = 1$ (a), 2 (b) and 2.9 (c) obtained in case III.

Disconnected edge midnode:

$$v_2 = (v_1 + v_7)/2, \qquad v_5 = (v_1 + v_{11})/2, \qquad v_6 = (v_1 + v_9)/2, \tag{11}$$

Disconnected face midnode:

$$v_3 = (v_1 + v_7 + v_8 + v_9)/4, \qquad v_4 = (v_1 + v_{11} + v_{10} + v_9)/4, \tag{12}$$

where v_i is the nodal velocity of node i. From Equations (11) and (12) an arbitrary velocity in element A is calculated by:

$$\begin{aligned} v_p &= N_3v_3 + N_{12}v_{12} + N_4v_4 + N_6v_6 + N_2v_2 + N_{13}v_{13} + N_5v_5 + N_1v_1 \qquad (13)\\ &= 0.25N_3v_8 + N_{12}v_{12} + 0.25N_4v_{10} + (0.25N_3 + 0.5N_6 + 0.25N_4)v_9 + (0.5N_2 + 0.25N_3)v_7 \\ &\quad + N_{13}v_{13} + (0.5N_5 + 0.25N_4)v_{11} + (N_1 + 0.5N_2 + 0.25N_3 + 0.5N_6 + 0.5N_5 + 0.25N_4)v_1 \end{aligned}$$

where N_i is the linear shape function of node i. Then, from Equation (13), the original connectivity [3, 12, 4, 6, 2, 13, 5, 1] is changed to [8, 12, 10, 9, 7, 13, 11, 1] and the shape functions [N_3, N_{12}, N_4, N_6, N_2, N_{13}, N_5, N_1] are replaced by [$0.25N_3$, N_{12}, $0.25N_4$, $(0.25N_3+0.5N_6+0.25N_4)$, $(0.5N_2+0.25N_3)$, N_{13}, $(0.5N_5+0.25N_4)$, $(N_1+0.5N_2+0.25N_3+0.5N_6+0.5N_5+0.25N_4)$]. And finally, after FEM analysis, nodal velocities of the disconnected nodes are obtained from Equations (12) and (13).

5. NUMERICAL ANALYSIS RESULTS OF PROBLEMS

To verify the efficiency of the marker surface method using an adaptive grid, the problems of radial flow with a point source and the collapse of a dam were analyzed in a three-dimensional co-ordinate system. The numerical results were compared with theoretical solutions, experimental results and other numerical results.

5.1. Radial flow from a point source

As shown in Figure 12, the radial flow from a point source involves fluid flow from a point source to a three-dimensional space with constant flowrate Q. The constant values of density, ρ, viscosity, μ, and flowrate, Q, used in the numerical analysis were 1, 1 and 4π respectively, and the time step Δt and the surface refinement level were given as 5.0×10^{-2} s, and 2 respectively. For three-dimensional analysis of this problem, as shown in Figure 12, the three-dimensional domain of 1/8 of a sphere near a point source was used. Since, from a theoretical viewpoint, this problem is a one-dimensional flow problem with only the radial velocity component, a theoretical solution exists. When it is assumed that steady state flow occurs at each time step, the theoretical solution in the spherical co-ordinates can be given by:

Table II. Comparison of results obtained in all cases

	Fine fixed grid	Fixed grid	Adaptive grid
Grid of flow field	2168	878	617
Average total number of elements			
Average total number of nodes	3017	1292	1107
Grid of total region	12 800	5000	1218
Average total number of elements			
Average total number of nodes	16 605	6630	2043
Relative length of edge side of element in front region	1.0	1.6	1.0
x-direction	1.0	1.0	1.0
y-direction			
z-direction	1.0	1.6	1.0
Relative total time	4.3	1.1	1.0

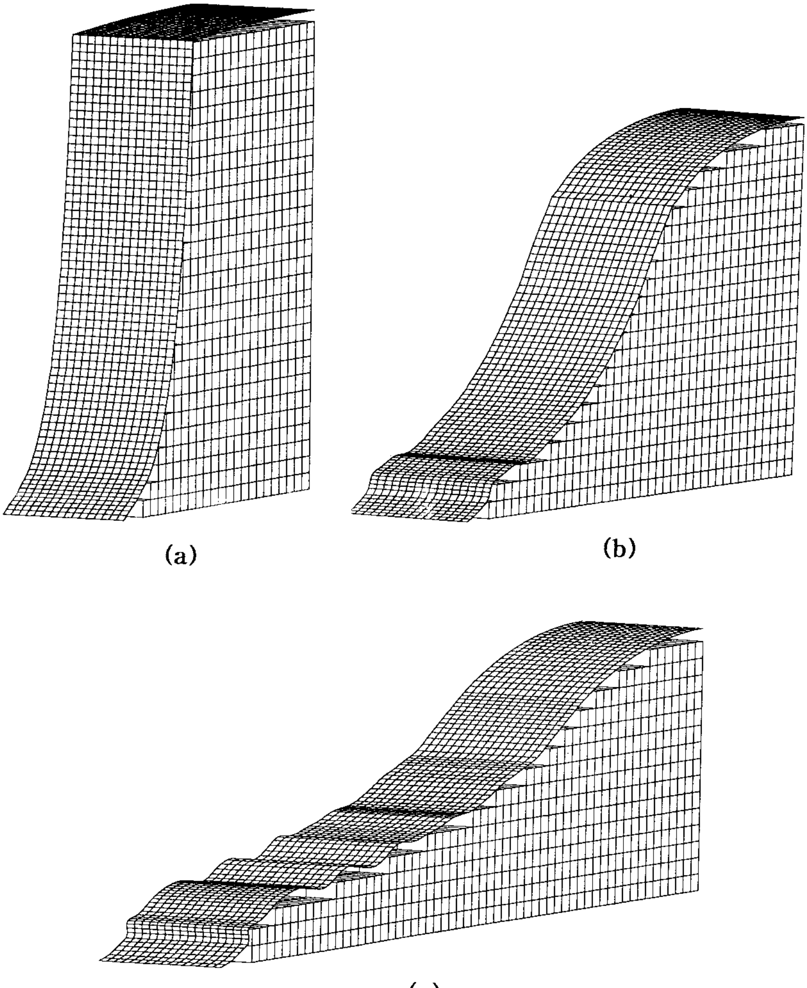

Figure 20. Predicted free-surfaces and element configurations at $T=1$ (a), 2 (b) and 2.9 (c) obtained in case I.

$$U_\mathrm{r}=\frac{Q}{4\pi r}, \qquad R=\sqrt{\frac{3Qt}{4\pi}+r_0^3}, \qquad P=-\frac{\rho Q^2}{2}(R^{-4}-r^{-4})-\frac{\mu Q}{\pi R^3}, \tag{14}$$

where U_r, r_0, r, R and P are the radial velocity, the initial and current radial distances from the point source, the position of the free-surface, and the pressure respectively.

This problem was analyzed with the fixed grid (case I) and the adaptive grid (case II). The initial grids of the total region for cases I and II are shown in Figure 13. The total number of elements of the initial grid for case I is about 14 times that of case II. In Figure 14, the adaptive grids to be regenerated at each time step for case II are shown. The predicted free-surfaces and element configurations for cases I and II are shown in Figure 15. Here, the surface elements including the marker surface were eliminated from the flow field grid for a more effective display. It can be seen from the adaptive grid of Figure 14, that the elements of the surface region are finer than those of other regions, and the surface refinement level, 2, is maintained at each time step. As shown in Figure 15, the marker surfaces for all cases can effectively represent the predicted free-surface in a three-dimensional co-ordinate system by the hidden-line removal treatment. And, by the marker surface refinement procedure, the sizes and shapes of marker surface elements of marker surface are maintained regularly at each time step. Also, it can be seen that while the elements in all regions are homogeneous for case I, the elements in the surface region of the flow field for case II are finer than those in other regions, since the flow field grid is created from the adaptive grid regenerated at each time step. In the surface region, as shown in Table I and Figure 15, the edge side length of an element for case II is about 2/3 times that of case I in the r-, θ- and ϕ-directions. Therefore, the flow field of case II can be constructed at each time step getting closer to the predicted free-surface than that of case I. Here, the level of each element near the boundary region, to which the inflow boundary condition is applied, maintains a value of 1 in order to prevent the change of the numerical quantity of the inflow flowrate by the coarsening procedure.

The free-surface positions predicted by the marker surface method in the spherical co-ordinate system for cases I and II are compared with the theoretical solution in Figure 16(a), and

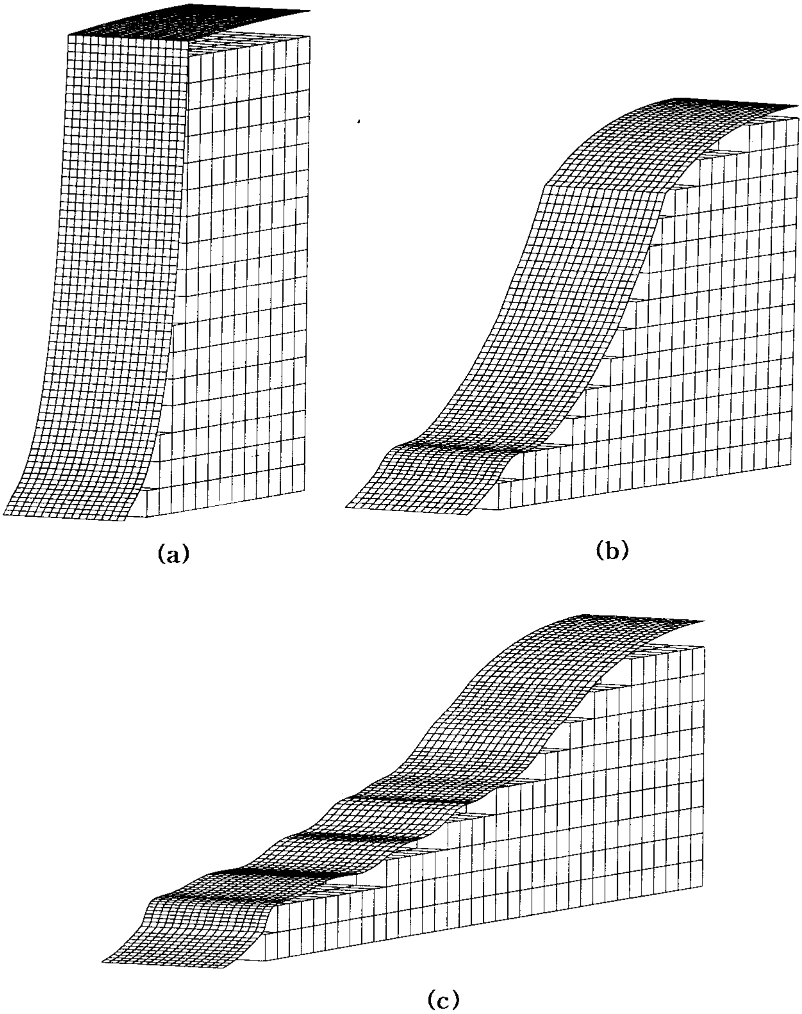

Figure 21. Predicted free-surfaces and element configurations at $T = 1$ (a), 2 (b) and 2.9 (c) obtained in case II.

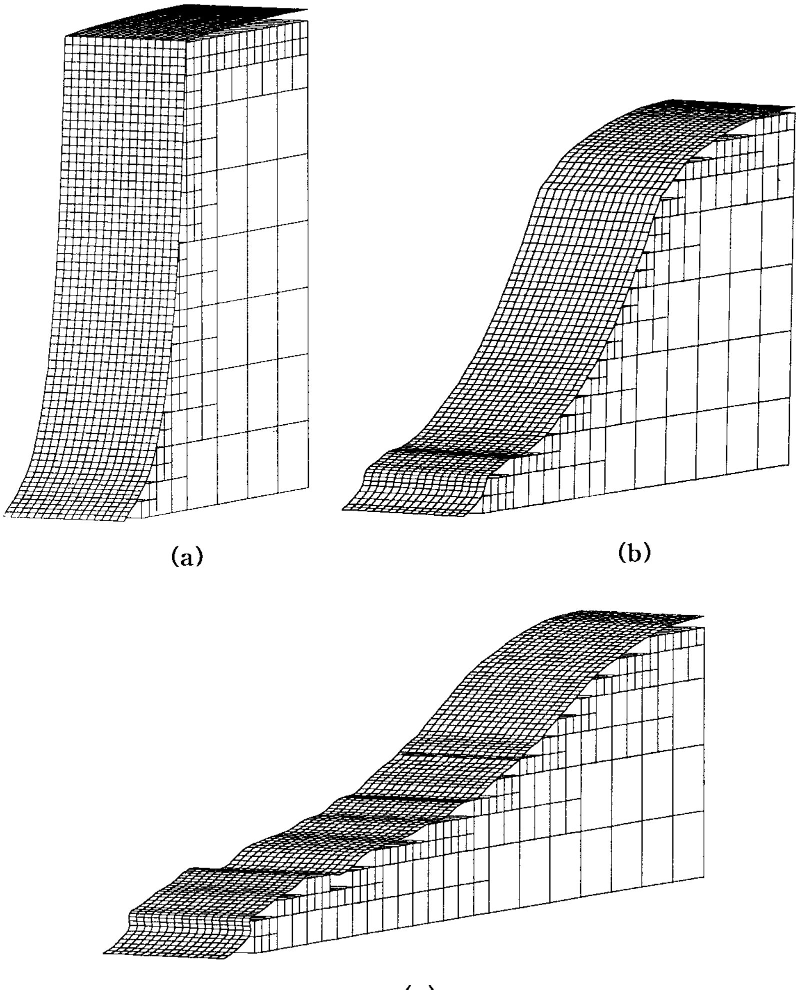

Figure 22. Predicted free-surfaces and element configurations at $T = 1$ (a), 2 (b) and 2.9 (c) obtained in case III.

the predicted pressures are compared with the theoretical solution in Figure 16(b). Figure 16(a) shows that the predicted positions for both cases are very close to the theoretical solution. However, as shown in Figure 16(b), the predicted pressure of case II is shown to be closer to the theoretical solution as compared with that of case I, and the waviness of case II has a smaller amplitude. The cause of such difference between the two cases is that the elements of case II are finer than those of case I, in the surface region, which is the most important region in the marker surface method. Also, the average values of the total number of nodes and elements and the total computation time for cases I and II are compared in Table I. Here, the total computation time for case II includes the time required for the construction of the adaptive grid by refinement and coarsening procedures. For the given problem, the construction of the adaptive grid required 12.7% of the total computation time. It should be noted that such a percentage is highly dependent on the numerical problem and the time steps used. The table shows that less memory size and shorter computation time were required for case II as compared with case I. This verifies the efficiency of the adaptive grid.

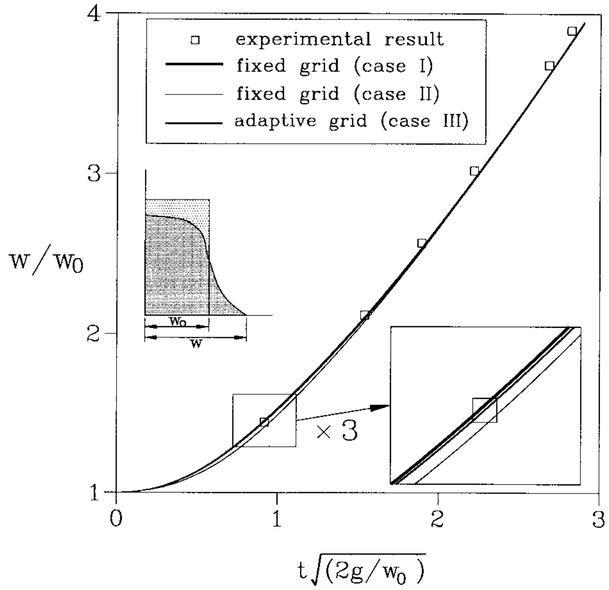

Figure 23. Predicted front position variation vs. time as compared with the experimental results by Martin and Moyce [20].

5.2. Collapse of a dam

For analysis of the collapse of a dam problem, three kinds of grids were used. Fixed grids were used for cases I and II, while an adaptive grid was used for case III. The numerical results of all cases were compared with the experimental results by Martin *et al.* [20] and the predicted free-surface shapes for cases II and III were compared with that of case I, which had the finest elements amongst the three cases. The number of elements of the total region in case II is about 39% of that for case I, and in case III, it is only 1/8 of it. As shown in Figure 17, the relative column height, b/a, is 2. The density of water, its viscosity and gravity are 1000

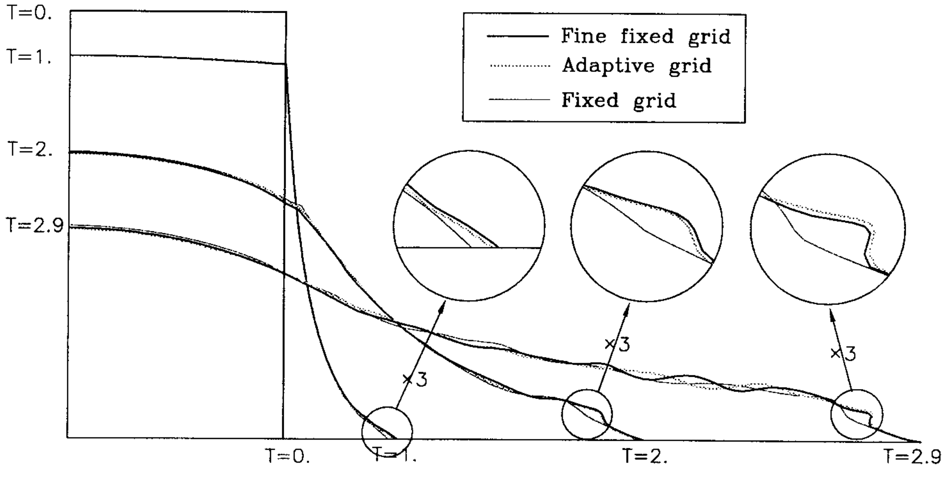

Figure 24. Comparison of predicted free-surfaces obtained in all cases.

$\mathrm{kg\,m^{-3}}$, 0.001 $\mathrm{kg\,m^{-1}\,s^{-1}}$ and 9.8 $\mathrm{m\,s^{-2}}$ respectively, and the time step Δt was taken to be 3.0×10^{-4} s and the surface refinement order as 2.

Figure 18 shows the initial grids for cases I, II and, III, and Figure 19 shows the adaptive grids generated for case III. In the surface region, as shown in Table II, the length of the edge side of an element of case II in the x- and y-directions is about 1.6 times of that for case I, while the length for case III is equal to that of case I. With the dimensionless time defined as $T = t\sqrt{2g/w_0}$, the element configurations of the flow field and the predicted free-surface at $T = 1$, 2 and 2.9 are shown in Figure 20 for case I. The elements of the flow field can be seen to be fine and the predicted free-surfaces, represented by the marker surface, can be seen to be very smooth and reasonable, since the elements of the initial grid are very fine. Figure 21 shows the results for case II. In comparison with case I, the predicted free-surface in regions near the wall are less accurate. And, from Figure 22, the results for case III, it can be seen that the flow field, where the elements in the surface region are fine, is constructed efficiently and that the predicted free-surfaces are predicted in a stable and effective manner. The positions of the predicted free-surface along the bed are compared with the experimental results of Martin *et al.* [20] in Figure 23. The predicted positions for cases I and III are very close to the experimental results. However, the numerical results for case II show some deviations from the experimental results since the element size is not sufficiently small to correctly predict the flow phenomenon in the collapse of a dam. In Figure 24. the predicted free-surface shapes for cases II and III are compared with that of case I. The predicted position of the free-surface for case III can be seen to be closer than that of case I, since finer elements were distributed in the free-surface region. The average values of the number of nodes and elements in the flow field and the total region, and the total computation time for all cases are shown in Table II. The largest amount of memory and computation time was required for case I, which used the largest number of elements in the initial grid. In case III, the smallest amount of memory and computation time was consumed because the elements of the grids in the flow field and the total region were used efficiently. For case III, 4.5% of the total computation time was consumed for the regeneration of the adaptive grids. These numerical results have shown that the proposed marker surface method and the adaptive grid can be used efficiently for the analysis of the dam collapsing problem.

6. CONCLUSIONS

In this work two features are incorporated for the improvement of numerical computation. First, a new marker surface method, in which the fluid flow is represented by the marker surface composed of marker elements instead of marker particles of the marker particle method, has been proposed. The marker surface was used in order to represent the free-surface accurately, to decrease the required memory and computation time, and to display the predicted three-dimensional free-surface as well. Secondly, an adaptive grid, which was created under a new criterion of element categorization of filling states, and the locations in the total region at each time step was incorporated in the marker surface method. The three-dimensional analyses of two problems, the radial flow with a point source and the collapse of a dam, have been carried out. The numerical results agreed well with the theoretical solutions and the experimental results as well. The results have verified the effectiveness of the proposed method and the efficiency of the adaptive grid. The marker surface method and adaptive grid refinement developed in this work can be further applied to a complex 3D example. Even though the present method allows the computation of a complex case, in the present work the validity of the proposed method is shown by employing the known examples with the analytic results or with the experimental data. The extension of the present work will be made in the ensuing work for complex three-dimensional examples.

REFERENCES

1. B. Ramaswamy and M. Kawahara, 'Lagrangian finite element analysis applied to viscous free-surface fluid flow', *Int. J. Numer. Methods Fluids*, **7**, 953–984 (1987).
2. F. Muttin, T. Coupez, M. Bellet and J.L. Chenot, 'Lagrangian finite element analysis of time-dependent viscous free-surface flow using an automatic remeshing technique: application to metal casting flow', *Int. J. Numer. Methods Eng.*, **36**, 2001–2015 (1993).
3. C.W. Hirt, A.A. Amsden and J.L. Cook, 'An arbitrary Lagrangian–Eulerian computing method for all flow speeds', *J. Comput. Phys.*, **14**, 227–253 (1974).
4. W.K. Liu, H. Chang, J.S. Chen and T. Belyischko, 'Arbitrary Lagrangian–Eulerian Petrov–Galerkin finite elements for non-linear continua', *Comput. Methods Appl. Mech. Eng.*, **68**, 259–310 (1988).
5. F.H. Harlow and J.E. Welch, 'Numerical calculation of time-dependent viscous incompressible flow of fluid with free-surface', *Phys. Fluids*, **8**, 2182–2189 (1965).
6. A.A. Amsden and E.H. Harlow, 'The SMAC method: a numerical technique for calculating incompressible fluid flows', *Los Alamos Scientific Laboratory Rep. LA-4370*, University of California, CA, 1970.
7. T. Nakavama and M. Mory, 'An Eulerian finite element method for time dependent free-surface problems in hydrodynamics', *Int. J. Numer. Methods Fluids*, **22**, 175–194 (1996).
8. C.W. Hirt, B.D. Nichols and N.C. Romero, 'SOLA-VOF: a solution algorithm for transient fluid flows', *Los Alamos Scientific Laboratory Rep. LA-5852*, University of California, CA, 1975.
9. C.W. Hirt and B.D. Nichols, 'Volume of fluid (VOF) method for the dynamics of free boundaries', *J. Comput. Phys.*, **39**, 201–225 (1981).
10. S.P. Wang and K.K. Wang, 'A net inflow method for incompressible viscous flow with moving free-surface', *Int. J. Numer. Methods Fluids*, **18**, 669–694 (1994).
11. W.S. Hwang and R.A. Stoehr, 'Molten metal flow pattern predicted for complete solidification analysis of net shape casting', *Mater. Sci. Technol.*, **4**, 240–250 (1988).
12. S. Chen, D.B. Johnson and P.E. Raad, 'The surface marker method', in *Computational Modeling of Free and Moving Boundary Problems*, *vol. 1*, *Fluid Flow*, de Gruyter, New York, 1991, pp. 223–234.
13. S.S. Wang and J. H. Stuhmliler, 'Modified partial-cell method for free-surface incompressible flow simulation', *Numer. Heat Transf.*, **3**, 209–223 (1980).
14. B.D. Nichols and C.W. Hirt, 'Calculating three-dimensional free-surface flows in the vicinity of submerged an exposed structures', *J. Comput. Phys.*, **12**, 234–246 (1973).
15. J.T. Oden, T. Strouboulis and P. Devloo, 'Adaptive finite element methods for the analysis of inviscid compressible flow: Part I. Fast refinement/unrefinement and moving mesh methods for unstructured meshes', *Comput. Methods Appl. Mech. Eng.*, **59**, 327–362 (1986).
16. P.R. Devloo, 'A three-dimensional adaptive finite element strategy', *Comp. Struct.*, **2**, 121–130 (1991).
17. J.H. Jeong and D.Y. Yang, 'Finite element analysis of transient fluid flow with free-surface using VOF (volume of fluid) and adaptive grid', *Int. J. Numer. Methods Fluids*, **26**, 1127–1154 (1998).
18. T.J.R. Hughes, Wing Kan Liu and A. Brooks, 'Finite element analysis of incompressible viscous flows by the penalty function formulation', *J. Comput. Phys.*, **30**, 1–60 (1979).
19. Noboru Kikuchi, *Finite Element Methods in Mechanics*, Cambridge University Press, New York, 1986.
20. J.C. Martin and W.J. Moyce, 'An experimental study of the collapse of liquid columns on a rigid horizontal plane', *Philos. Trans. Ser. A*, *Math. Phys. Sci.*, **244**, 312–324 (1952).